Investigation of Caves under Complicated Engineering Geological Conditions using High-density Resistivity Method

Yekai Men (menyekai@neuq.edu.cn)
Northeastern University https://orcid.org/0000-0002-6178-7615
Ende Wang
Northeastern University
Jianfei Fu
Northeastern University
Kai Guo
Northeastern University
Xinwei You
Northeastern University

Research Article

Keywords: underground cave, high-density resistivity method, forward model, inversion calculation

Posted Date: June 9th, 2021

DOI: https://doi.org/10.21203/rs.3.rs-161423/v1

Investigation of Caves under Complicated Engineering Geological Conditions using High-density Resistivity Method

Yekai Men [1,2,*], Ende Wang[1,3], Jianfei Fu [1,3] , Kai Guo [3], Xinwei You [3]

[1] *Key Laboratory of Ministry of Education on Safe Mining of Deep Metal Mines, Northeastern University, Shenyang 110819 and China;*

[2] *School of Resource and Materials, Northeastern University at Qinhuangdao, Qinhuangdao 066004, China;*

[3] *School of Resource and Civil Engineering, Northeastern University, Shenyang 110819, China;*

*Corresponding author: Yekai Men

NO. 143, Taishan Road, Economic and Technological Development District,

Qinhuangdao 066004, Hebei Province, P.R. China.

Tel.: +86 335 805 7908; Fax: +86 335 805 7908

E-mail: menyekai@neuq.edu.cn

Abstract

It is a difficult problem to accurately survey underground caves in the regions characterized by complicated engineering geological and sophisticated geophysical conditions. The cave of Yuanjiacun iron mine features various sedimentary facies and is the focus area for this study. A high-density resistivity method is used to study the accurate survey methods of the cave under complicated engineering geological conditions. The resistivity of the iron ore in the major sedimentary facies is measured using the outcrop method. The results indicate significant resistivity differences among different sedimentary facies. The oxide facies has a high resistivity, and the silicate facies has a low resistivity. Cave investigation forward models for the caves that occur in each sedimentary facies are developed. The forward calculations identify the resistivity anomalies of the caves for the various sedimentary facies. Furthermore, the resistivity characteristics are more evident in the low-resistivity silicate sedimentary facies. Differences in the reflection of caves exist among different arrays, particularly the dipole array more evident. The high-density resistivity method is used to survey the site and the potential safety risks are eliminated by accurately identifying two caves by their resistivity anomaly characteristics.

Keywords: underground cave; high-density resistivity method; forward model; inversion calculation

1. Introduction

Accurate surveys of hidden underground caves are important for geological engineering investigations. Currently, geophysical prospecting and engineering drilling are the main methods used for underground cave surveys; other supporting methods are also available, including ground deformation observations, hydrological tests and microseismic monitoring. Several studies have used geophysical prospecting techniques on underground cavities in karst areas. Martínez-Moreno et al. (2013) advanced these methods by surveying deep limestone caves in the Estepa Mountains using microgravity and electrochromatography techniques. Gómez-Ortiz and Martín-Crespo (2012) identified hidden caves around a dolomite subsidence area in Madrona (Spain) using ground penetrating radar and resistivity tomography. Gambetta et al. (2011) studied the geophysical response of the shallow caves under complicated geological environments in the karst area of the Ameta Mountains (Italy) using the vertical gravity gradient and resistivity tomography. Abu-Shariah (2009) outlined the geometry of the underground cavities in Batu Caves in Kuala Lumpur using 2D resistivity imaging technology. Park et al. (2010) mapped the 3D spatial distribution of the karst caves in Yongweili on the southwest Korean Peninsula using a 2D resistivity method and 3D gravimetry. Such survey regions, which are all limestone areas with a simplex lithology, feature simple engineering geology and geophysical characteristics. However, the geophysical fields are complicated and changeable due to the different geophysical properties of strata of different lithologies, leading to a significant uncertainty in identifying the cave anomaly.

Many large-scale mines in China are severely affected by hidden underground caves (Zhang et al., 2009; Xu et al., 2006; Dai et al., 2010; Men et al., 2010). The special geology and geologic processes create various deposits (Goldfarb et al., 2001). Such mines have more complicated engineering geological conditions than karst areas have, making them the

favorable sites for accurate surveys of underground caves in areas of complicated engineering geological conditions. Zhang et al. (2009) studied caves of a gold mine using high-precision gravity measurements. Xu et al. (2006) surveyed a hidden cave containing water using the seismic transverse wave reflection method. Dai et al. (2010) performed an integrated survey and investigation in a molybdenum mineral cave using ground penetrating radar and EH4 conductivity imaging. However, such studies, surveys and investigations have all ignored how complicated geological conditions interfere with the identification of cave anomalies, which impairs the practical applications of the research findings.

The Yuanjiacun iron mine in, Shanxi Province, China is an open-pit iron mine with the largest production scale in Asia (up to 80 Mt/a ore prodution), which has been frequently and severely plagued by potential caves. The iron ores of all sedimentary facies, which are common in the banded iron formation (BIF) iron mine (Klein, 2005), are developed there. The iron ores from different sedimentary facies vary in their mineral composition and resistivity; therefore, the complicated and changeable geoelectric section greatly interferes with the accurate survey of caves. The high-density resistivity method is used to study the survey of caves under complicated engineering geological conditions in the Yuanjiacun iron mine. The finite element method is applied to forward modeling of the constructed cave model. This study has laid the theoretical basis for the accurate delineation of caves and has achieved favorable results in the field survey.

2. Geological Setting of the Study Area

The Yuanjiacun iron mine is located at the western margin of the middle of central collisional orogenic belt of North China Craton, within the meta-sedimentary rocks of the early Proterozoic Lvliang Group (Wang et al., 2015). Overall, the deposit has a NNE-near SN strike, with a SE-E trend of 60°~80° (Fig. 1a). The mine is 6 km in length from south to north and 0.4~1.5 km in width from east to west. There are a total of 20 orebodies of different

sizes, among which No. 10 and No. 1 are the largest. The major orebodies are stratiform-like. A few are lenticle-like and irregular (Fig. 1b). The ore structures mainly include stripped and ribbon patterns, followed by hole and massive patterns. The mineral composition is sophisticated. The metallic minerals include the major iron oxides (e.g., magnetite, martite or semi-martite, hematite, specularite) and a few examples of siderite and infinitesimal pyrite and chalcopyrite. The major nonmetallic minerals include quartz and silicate minerals (e.g., cummingtonite, minnesotaite and stilpnomelanite), followed by carbonate minerals.

Based on the paragenetic assemblage of the original minerals, the iron ore is divided into three primary sedimentary facies; i.e., the oxide, silicate and carbonate facies. The oxide facies is dominant and is further divided into the magnetite subfacies (Fig. 2a) and the hematite subfacies (Fig. 2b) based on the type of oxide. The representative ore types are quartzose magnetite and quartzose hematite. The major mineral composition of the former includes quartz and magnetite. The major mineral composition of the latter includes quartz and hematite. The ore body of the silicate facies is characterized by a large amount of silicate minerals, including stilpnomelanite, cummingtonite, actinolite and chlorite. This sedimentary facies is further divided into the cummingtonitic magnetite subfacies (Fig. 2c) and the cummingtonitic hematite subfacies (Fig. 2d). Cummingtonitic magnetite and cummingtonitic hematite are the primary components of the former and the latter, respectively. The main minerals of the carbonate facies are siderite and ankerite, which are sporadically distributed in the south part of the study area, with no independent industrial ore body developed.

3. Forward Modeling of Caves

3.1. Forward calculation method

Forward modeling of the high-density resistivity method is essential for characterizing the final spatial distribution of the stable current field of underground. This method calculates

the apparent resistivity that corresponds to a specific array form based on the potential value of each point obtained by the flow field of stable points determined by numerical simulation, provided that the geologic model and the initial boundary conditions are known (Inoue et al., 2016). In practice, the finite element method, finite difference method and conformal mapping method are commonly used to handle the geophysical field simulation in a sophisticated geoelectric model. The finite element method is applicable to a scenario that has a complicated distribution of the physical property parameters and a rolling topography in which the approximate complex geometrical boundary is close to the actual situation (Liu, 2007). The finite element method is used for forward modeling.

To solve the potential of a stable current field, the target boundary value problem must be converted into the corresponding variational problem based on the variational principles to calculate the functional minimum (Feng et al., 2014; Rucker et al., 2009; Mukanova and Orunkhanov, 2010). Subjected to the 2D geoelectric conditions, the point current source field is calculated to determine the boundary value of the 2D partial differential equation of the Fourier transform $V(\lambda, x, z)$ for the potential of several given values of λ waves, as shown in formula 1, as follows:

$$\begin{aligned} &\frac{\partial}{\partial x}(\sigma\frac{\partial V}{\partial x})+\frac{\partial}{\partial z}(\sigma\frac{\partial V}{\partial z})-\lambda^2\sigma V=f_1 \\ &\left.\frac{\partial V}{\partial n}\right|_{\Gamma_1}=0 \\ &\left[AV+\frac{\partial V}{\partial n}\right]_{\Gamma_2}=0 \end{aligned} \tag{1}$$

where $f_1=-\sum_{k=1}^{n} I_k\delta(x-x_k,z-z_k)$, and I_k is the current source strength of Point k.

The variational problem that is equivalent of the boundary value problem of the 2D partial differential equation is, as follows:

$$J\ (V) = \iint \left\{ \sigma \left[\left(\frac{\partial V}{\partial x} \right)^2 + \left(\frac{\partial V}{\partial z} \right)^2 + \lambda^2 V^2 \right] + 2 f_1 \cdot V \right\} ds + \int_{\Gamma_2} \sigma A V^2 dl = \min \tag{2}$$

Second, the continuous solution area is discretized, and the solution area is divided into several grid cells interlinked at the nodes according to certain rules that approximately discretize the variation equation for each cell (Sasaki, 1994). As for the 2D variation, the upper functional value of the divided cell is calculated by linear interpolation of function V in cell $J_e(V)$. The functional value of the whole area $J(V)$ is the sum of the values $J_e(V)$ of all cells, as shown in Formula 3:

$$J(V) = \sum_{e=1}^{N} J_e(V) \tag{3}$$

After the cell analysis and combination, the continuous variational problem is discretized to develop a high order linear equation set with the potential value of each node as the variation, as follows:

$$K\vec{V} = \vec{I} \tag{4}$$

where K refers to the overall stiffness matrix, with the sum of all unit stiffness matrices as the element K^e, i.e., $K = \sum_{e=1}^{N} K^e$;

$\vec{I}$ is the power supply point related vectors; and

$\vec{V}$ is the Fourier potential to be calculated.

This equation is solved to obtain the Fourier potential of each node corresponding to several different numbers of waves λ. Then, the Fourier inversion is used within Formula 5 to calculate the potential (U) of each node (Liu, 2007; Tripp et al., 1984), as follows:

$$U（x,o,z）=\frac{2}{\pi}\int_0^{\infty}V(x,\lambda,z)d\lambda \tag{5}$$

The apparent resistivity is calculated by Formula 6 (Liu, 2007). By observing the change law of the apparent resistivity, the existence and distribution of the underground geologic body with the electrical heterogeneity are used to define the distribution of the half-space field below the surface to characterize the spatial distribution of the stable current field.

$$\rho_s = K\frac{\Delta U_{MN}}{I} \tag{6}$$

where K refers to the coefficient of array.

3.2. Resistivity test

The mini-four-electrode array on outcrops can be used to determine the resistivity of rocks in the field (Liu, 2007). The resistivity values of the main rocks and orebodies of different sedimentary facies in the study area are tested by this method. The resistivity distribution diagram is developed from the measured data (Fig. 3), indicating the greatest resistivity of the oxide facies ore among all those in the mining area. The resistivity range of the quartzose magnetite is 1,738-5,231 Ω·m, with an average of 3,060 Ω·m; the resistivity range of quartzose hematite is 1,018-4,192 Ω·m, with an average of 2,150 Ω·m. The resistivity is significantly reduced in the silicate facies due to the large amount of silicate minerals in the ores of the silicate facies. The resistivity range of the cummingtonitic magnetite is 935-2,237 Ω·m, with an average of 1,460 Ω·m; the resistivity range of cummingtonitic hematite is 509-1,134 Ω·m, with an average of 810 Ω·m. The intercalated diabase, which is common in the ore body, has a resistivity range of 785-2,558 Ω·m, with an average of 1,550 Ω·m. The schist which is the main surrounding rock of the ore body has the lowest resistivity, which ranges from 435 to 1,224 Ω·m, with an average of 770 Ω·m.

3.3. Modeling and forward calculation

A cave-free geoelectric model is developed based on the geologic features of the ore body (Fig. 4c). The average of the measured resistivity is selected as the resistivity of each geologic body in the model. The distribution area of schist is setted to be within 0~10 m of the horizontal surface distance; that of quartzose magnetite is within 10~57 m; that of quartzose hematite is within 57~102 m; that of diabase is within 102~110 m; that of cummingtonitic magnetite is within 110~153 m; that of cummingtonitic hematite is within 153~223 m; and that of diabase is within 223~264 m. As shown in the Wenner Array Resistivity Section of the forward model (Fig. 4a), the low-resistivity anomaly area reflecting the schist is identified within a horizontal distance of 0~11.5 m. The high-resistivity anomaly area reflecting the quartzose magnetite is identified within 11.5~60 m. The secondary high-resistivity anomaly area reflecting the quartzose hematite is identified within 60~102 m. The anomaly free areas reflecting the diabase are identified within 102~108 m and 156~220 m. The low-resistivity anomaly area reflecting the cummingtonitic hematite is identified within 108~156 m. The secondary low-resistivity anomaly area reflecting the cummingtonitic magnetite is identified within 153~223 m. The forward calculation indicated the significant resistivity response of each geologic body in the resistivity section and the approximately consistent spatial distribution of both the resistivity anomaly and the geologic body. Therefore, the spatial distribution of each geologic body can be defined according to the spatial distribution characteristics of resistivity. As shown in the resistivity section of the Dipole Array (Fig. 4b), overall, the spatial distribution range of each geologic body can be differentiated, although there is deviation between the resistivity features of each geologic body by the Wenner Array.

Based on the cave-free survey model, the corresponding cave survey models are successively developed by assuming that the caves occur in the orebodies of different sedimentary facies. The site survey indicated that the caves in the survey area are well preserved and are not filled with underground water, with little collapse or gravel filling.

Therefore, the caves in the survey area may be considered insulators with an extremely high resistivity, which is set to be 100,000 Ω·m. The horizontal surface distance and depth of the cave in the cummingtonitic magnetite are set to 174~195 m and 15~30 m, respectively (Fig. 5c). As shown in the resistivity section developed by forward calculation (Fig. 5a, b), the resistivity anomaly features reflecting the cummingtonitic magnetite change significantly compare with that of the cave-free case. The high-resistivity anomaly area is apparent in the range of the amphibolic magnetite. This anomaly position approximately conforms to the set location of the cave, indicating the reflection of this anomaly area in the resistivity section of the cave. Compared with the Wenner Array, the cave anomaly is greatly manifested within the Dipole Array.

The horizontal surface distance and depth of the cave in the cummingtonitic hematite are set to 126~147 m and 15~30 m, respectively (Fig. 6c). As shown in the Dipole Array resistivity section developed by forward calculation (Fig. 6b), the significant high-resistivity anomaly area is identified in the range of the cummingtonitic hematite compared with that of the cave-free case. This anomaly position approximately conforms to the location of the cave, indicating the reflection of this anomaly area in the resistivity section of the cave. No significant high-resistivity anomaly is identified in the Wenner Array resistivity section (Fig. 6a). However, the resistivity of the cummingtonitic hematite is greater than that of the cave-free scenario, indicating the reflection of the anomaly of cave in the Wenner Array resistivity section.

The horizontal surface distance and depth of the cave in the quartzose hematite are set to be 75~96 m and 15~30 m, respectively (Fig. 7c). As shown in the Wenner Array resistivity section developed by forward calculation (Fig. 7a), the resistivity of the quartzose hematite is greater than that of the cave-free scenario, indicating the reflection of the cave. The cave anomaly is clearly reflected in the Dipole Array resistivity section (Fig. 7b). The high-resistivity anomaly area of the cave is identified in the range of quartzose hematite, and

the spatial location of the anomaly area is approximately consistent with the set location of the cave.

The horizontal surface distance and depth of the cave in the quartzose magnetite are set to 27~48 m and 15~30 m, respectively (Fig. 8c). As shown in the Dipole Array resistivity section developed by forward calculation (Fig. 8b), the significant high-resistivity anomaly area is identified in the range of the quartzose magnetite compared with that of the cave-free scenario, indicating the existence of a cave. however, as shown in the Wenner Array resistivity section (Fig. 8a), the high-resistivity anomaly distribution changes to some extent, which indicates the existence of caves.

In conclusion, the caves occur in the orebodies of different sedimentary facies, with the anomaly reflected in the resistivity section. If a cave occurs in the ore body of the low-resistivity silicate facies, the cave anomaly may be obviously reflected in the resistivity sections of both devices. If a cave occurs in a ore body of the comparatively high resistivity oxide facies, the Dipole Array reflects better than the Wenner Array.

4. Survey Examples

The survey area is in the open pit of the Yuanjiacun iron mine (Fig. 2e). The survey lines for high-density resistivity method are arranged according to the geologic features and the site conditions of the deposit (Fig. 2f). In total, 4 survey lines are arranged, each of which is subvertical to the orebody strike (Fig. 9). From the starting point, the survey lines pass through quartzose hematite, diabase, cummingtonitic magnetite, diabase, quartzose magnetite, schist and quartzose hematite. The schists, vein rocks and orebodies of almost all the sedimentary facies occur in the survey area, leading to the complicated geological conditions. Based on the forward model, the Dipole Array with better resistivity anomaly reflection is selected for the survey. There are 75 electrodes installed on each line every 3 m.

241 The segregation coefficient is 20 and the space between the survey lines is approximately 20
242 m.

243 Inversion of the measured data is carried out to develop the inversion section of
244 resistivity (Fig. 10). Figure 10a, b show the resistivity inversion sections of the survey line
245 GY-4 and GY-3, respectively. The resistivity reflections of the ore body of each sedimentary
246 facies, diabase and schist vary significantly in the resistivity sections. The spatial distribution
247 of resistivity in each geologic body approximately matches the actual geological data (Fig.
248 10a). Several high-resistivity anomalies in the section are reflections from high resistivity
249 quartzose magnetite. No cave exists in the layout range of the survey lines. Figure 10c, d
250 show the resistivity inversion sections of the survey lines GY-2 and GY-1, respectively. The
251 resistivity distribution characteristics of GY-2 and GY-1 change significantly, comparing
252 with that of GY-4 and GY-3. In addition to the distribution features of each geologic body
253 reflected by the features of the resistivity, 2 high-resistivity anomalies exist in the distribution
254 areas of cummingtonitic magnetite and quartzose magnetite and are speculated to be the
255 reflection of the cave anomaly. According to the cave anomaly features of GY-2, two
256 boreholes (ZK-1 and ZK-2) are set at the anomaly centers (horizontal distance of 78 m and
257 132 m, respectively) for verification (Fig. 10c). The caves are identified by drilling at depths
258 of 21 m and 13 m, respectively. Accurate spatial information of the caves is obtained using
259 3D models of the caves (Fig. 10e, f) developed by 3D laser scanning, which further improves
260 the precision of the cave survey to less than 0.5m and provides reliable references for future
261 treatment of caves.

262 ## 5. Conclusions

263 1) Significant resistivity differences are identified among orebodies of each sedimentary
264 facies. The ore body of the oxide facies has a relatively high resistivity, and the ore body of
265 the silicate facies has a relatively low resistivity.

2) According to forward modeling, the reflection features of the resistivity anomaly are more obvious if the caves occur in the ore body of a low resistivity silicate facies. Compared with the Wenner Array, the cave anomaly is more sensitive to reflection by Dipole Array.

3) Accurate spatial information of the underground hidden cave is obtained from the resistivity section anomaly features identified by inversion, combining drilling verification and 3D laser modeling results. This study shows that this method may accurately identify the hidden caves in iron mines with complicated sedimentary facies, eliminating safety risks during production.

Declarations

Funding: National Key Research and Development Program (No. 2016YFC0801603, 2017YFC1503105); Fundamental Research Funds for the Central Universities (No. N172303015); Scientific Research Fund of Northeastern University at Qinhuangdao (No. XNB201720).

Conflict of interest: The authors declare that they have no conflict of interest. All co-authors have seen and agree with the contents of the manuscript, and there is no financial interest to report. We certify that the submission is original work and is not under review at any other publication.

Availability of data and material: The datasets used or analysed during the current study are available from the corresponding author on reasonable request.

Code availability: Not applicable

Authors' contributions: Yekai Men performed the data analyses and wrote the manuscript; Ende Wang contributed to the conception of the study; Jianfei Fu contributed significantly to analysis and manuscript preparation; Kai Guo and Xinwei You performed the experiment.

Acknowledgements

This research was financially supported by the National Key Research and Development Program (No. 2016YFC0801603, 2017YFC1503105), Fundamental Research Funds for the Central Universities (No. N172303015), and Scientific Research Fund of Northeastern University at Qinhuangdao (No. XNB201720).

References

Abu-Shariah, M. I. I. 2009. Determination of cave geometry by using a geoelectrical resistivity inverse model. Engineering Geology, 105, 239-244.

Dai, Q. W., Xu, K., Feng, D. S., Zhang, B. 2010. The application of ground penetrating radar and EH4 in goaf exploration. Progress in Geophysics, 25, 1763-1768. (In Chinese with English abstract)

Feng, D. S., Dai, Q. W., Xiao, B. 2014. Contrast between 2D inversion and 3D inversion based on 2D high-density resistivity data. Transactions of Nonferrous Metals Society of China, 24, 224-232.

Gambetta, M., Armadillo, E., Carmisciano, C., Stefanelli, P., Cocchi, L., Tontini, F. C. 2011. Determining geophysical properties of a near-surface cave through integrated microgracity vertical gradient and electrical resistivity tomography measurements. Journal of Cave and Karst Studies, 73, 11-15.

Goldfarb, R. J., Groves, D. I., Gardoll, S. 2001. Orogenic gold and geologic time: a global synthesis. Ore Geology Reviews, 18, 1-75.

Gómez-Ortiz, D., Martín-Crespo, T. 2012. Assessing the risk of subsidence of a sinkhole collapse using ground penetrating radar and electrical resistivity tomography. Engineering Geology, 149-150, 1-12.

Inoue, K., Nakazato, H., Kubota, T., Takeuchi, M., Sugimoto, Y., Kim, H. J., Furue, K. 2016. Three-dimensional inversion of in-line resistivity data for monitoring a

groundwater recharge experiment in a pyroclastic plateau. Exploration Geophysics, 48, 332-343.

Klein, C. 2005. Some Precambrian banded iron-formations (BIF) from around the world: Their age, geologic setting, mineralogy, metamorphism, geochemistry, and origins. American Mineralogist, 90, 1473-1499.

Liu, T. Y. 2007. Conspectus of geophysical exploration. Beijing: Geological Publishing House. (In Chinese with English abstract)

Martínez-Moreno, F. J., Pedrera, A., Ruano, P., Galindo-Zaldívar, J., Martos-Rosillo, S., González-Castillo, L., Sánchez-Úbeda, J. P., Marín-Lechado, C. 2013. Combined microgravity, electrical resistivity tomography and induced polarization to detect deeply buried caves: Algaidilla cave (Southern Spain). Engineering Geology, 162, 67-78.

Men, Y. K., Fan G. H., Shao A. L., Jia, S. S., Wang, E. D, Yang, Y. B. 2010. The Study of Integrated Detection Method to the Mined-out Areas in Open Pit Iron Mine and its Application, Metal Mine, 39, 124-127. (In Chinese with English abstract)

Mukanova, B., Orunkhanov, M. 2010. Inverse resistivity problem: Geoelectric uncertainty principle and numerical reconstruction method. Mathematics and Computers in Simulation, 80, 2091-2108

Park, G., Park, S., Yi, M., Rim, H., Cho, S., Kim, J. 2010. Geostatistical integration using 2-D electrical resistivity and 3-D gravity methods for detecting cavities in a karst area. Environmental Earth Sciences, 60, 965-974.

Rucker, D. F., Levitt, M. T., Greenwood, W. J. 2009. Three-dimensional electrical resistivity model of a nuclear waste disposal site. Journal of Applied Geophysics, 69, 150-164.

Sasaki, Y. 1994. 3-D resistivity inversion using the finite-element method. Geophysics, 59, 1839-1848.

341 Tripp, A. C., Hohmann, G. W., Swift, C. M. 1984. Two-dimensional resistivity inversion.
342 Geophysics, 49, 1708-1717.
343 Wang, C., Zhang, L., Dai, Y. & Lan, C.Y. 2015b. Geochronological and geochemical
344 constraints on the origin of clastic meta-sedimentary rocks associated with the
345 Yuanjiacun BIF from the Lüliang Complex, North China. Lithos, 212-215, 231-246.
346 Wang ,C. L., Zhang, L. C., Lan, C. Y., Dai, Y. P. 2014. Rare earth element and yttrium
347 compositions of the Paleoproterozoic Yuanjiacun BIF in the Lüliang area and their
348 implications for the Great Oxidation Event (GOE). Science China: Earth Sciences 57,
349 2469-2485.
350 Xu, B. S., Wang, E. D., Tian, G., Han, J. 2006. Detecting underground water-bearing caves
351 by seismic transverse wave reflection method. Journal of Northeast University (Natural
352 Science), 27, 84-87. (In Chinese with English abstract)
353 Zhang, S. F., Meng. L. S, Du, X. J., Zhang, F. X., Ma, G. Q. 2009. Study on the application
354 of high precision gravity survey in detecting mined-out areas of gold mines. Progress
355 in Geophysics, 24, 590-595. (In Chinese with English abstract)

Figure captions

Figure 1. (a) Geological map of the Yuanjiacun BIF and (b) profile of the IV prospecting line (after Wang et al., 2014).

Figure 2. (a) Quartzose magnetite; (b) Photomicrograph of quartzose hematite (reflected light); (c) Photomicrograph of cummingtonitic magnetite (reflected light); (d) Cummingtonitic hematite; (e) Lithology variation in research area; (f) Field data collection. (Hem – hematite; Qtz – quartz; Mag – magnetite; Stp – stilpnomelane).

Figure 3. Resistivity distribution of main rocks and ores.

Figure 4. Cave-free survey model.

Figure 5. Survey model with caves in cummingtonitic magnetite.

Figure 6. Survey model with caves in cummingtonitic hematite.

Figure 7. Survey model with caves in quartzose hematite.

Figure 8. Survey model with caves in quartzose magnetite.

Figure 9. Survey line layout of the high-density resistivity method.

Figure 10. Resistivity inversion section of each survey line.

Figures

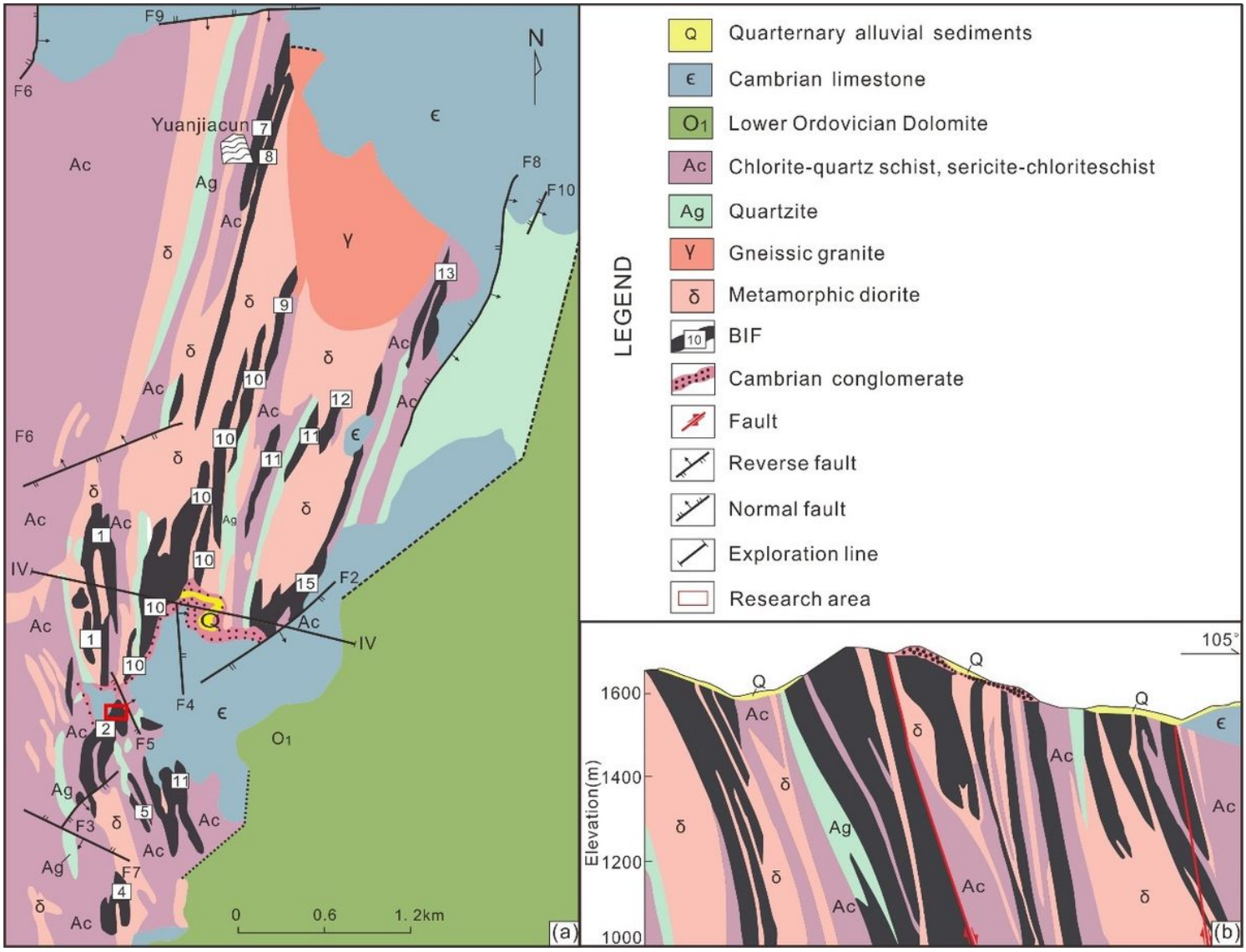

Figure 1

(a) Geological map of the Yuanjiacun BIF and (b) profile of the IV prospecting line (after Wang et al., 2014). Note: The designations employed and the presentation of the material on this map do not imply the expression of any opinion whatsoever on the part of Research Square concerning the legal status of any country, territory, city or area or of its authorities, or concerning the delimitation of its frontiers or boundaries. This map has been provided by the authors.

Figure 2

(a) Quartzose magnetite; (b) Photomicrograph of quartzose hematite (reflected light); (c) Photomicrograph of cummingtonitic magnetite (reflected light); (d) Cummingtonitic hematite; (e) Lithology variation in research area; (f) Field data collection. (Hem – hematite; Qtz – quartz; Mag – magnetite; Stp – stilpnomelane).

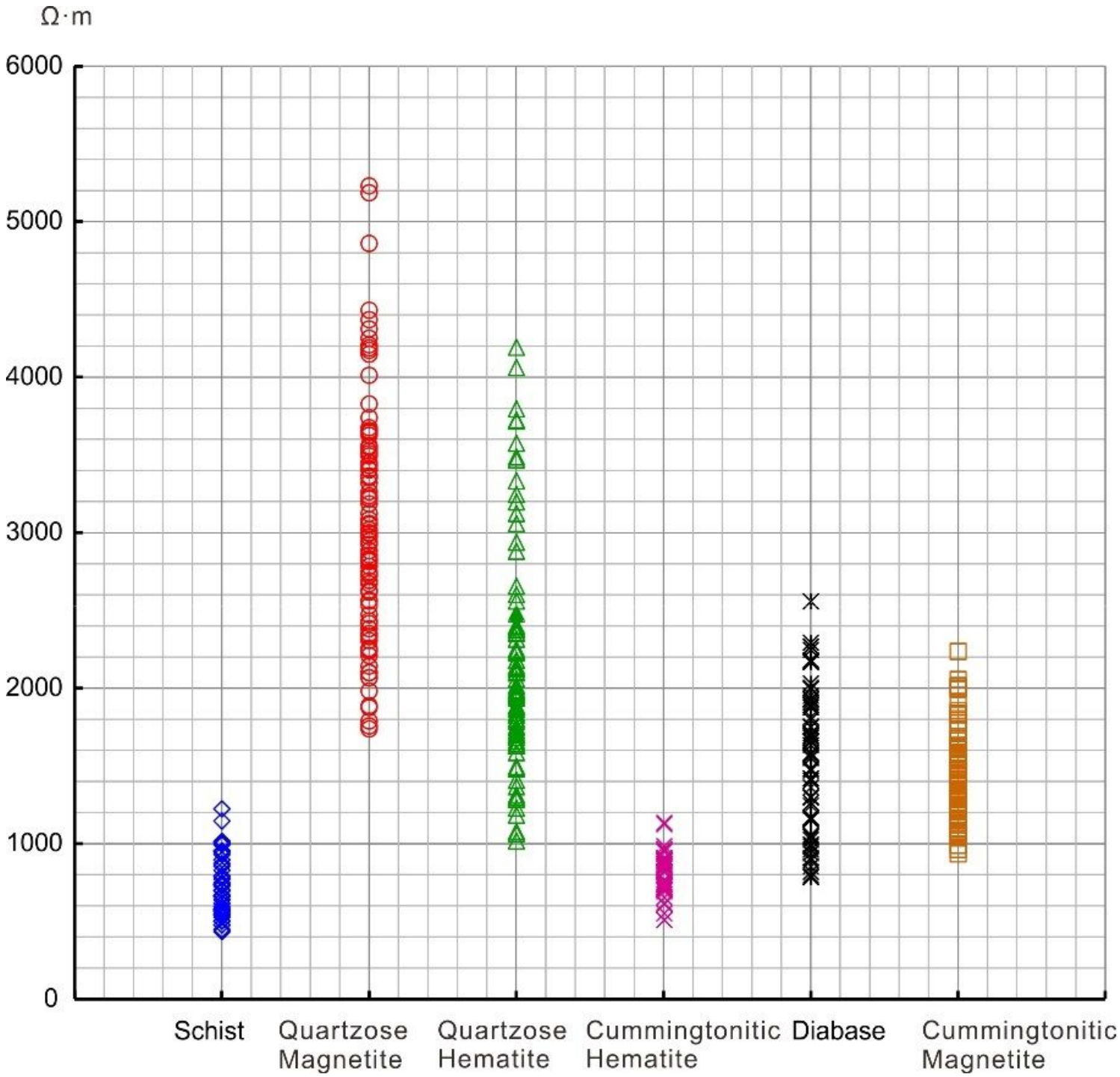

Figure 3

Resistivity distribution of main rocks and ores.

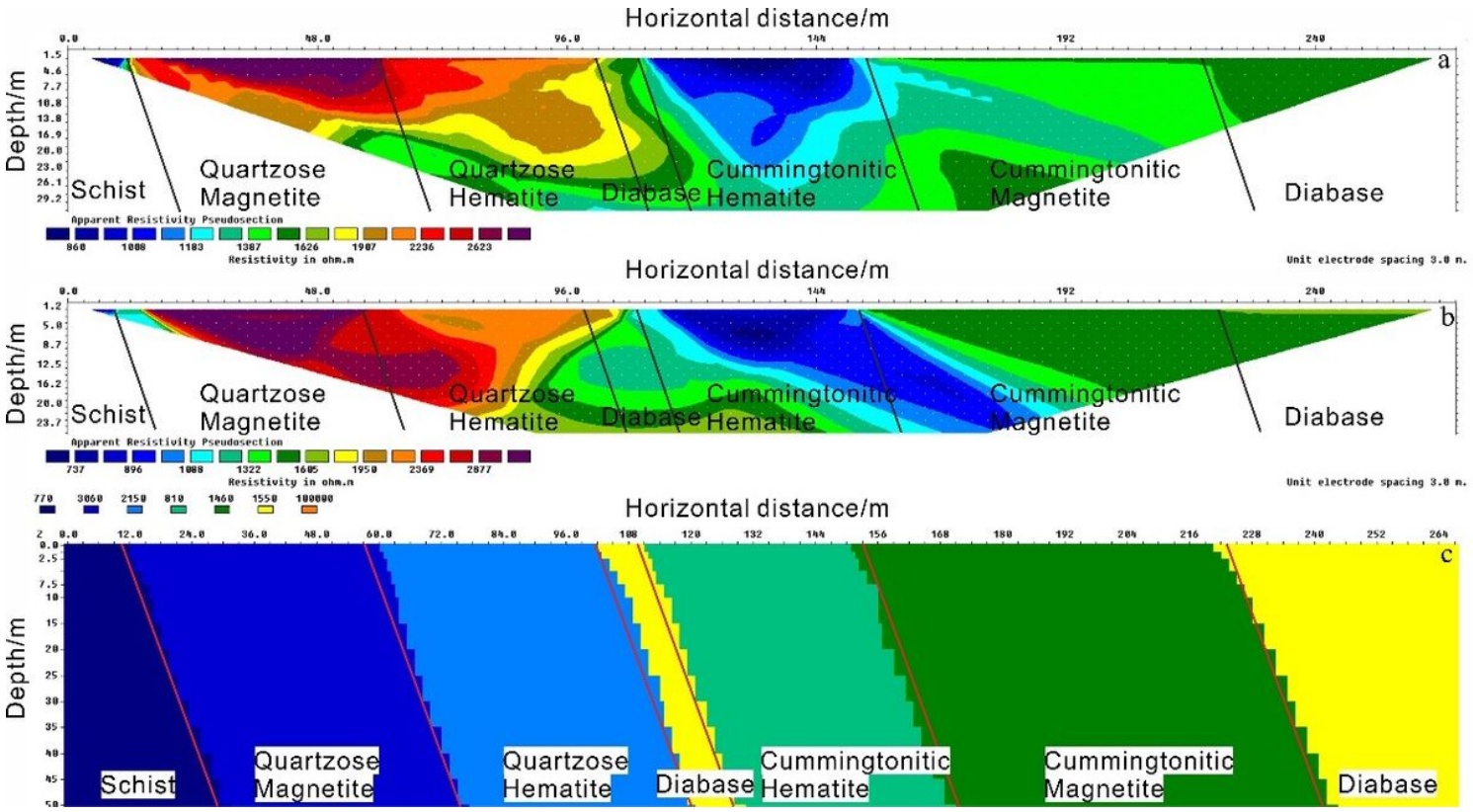

Figure 4

Cave-free survey model.

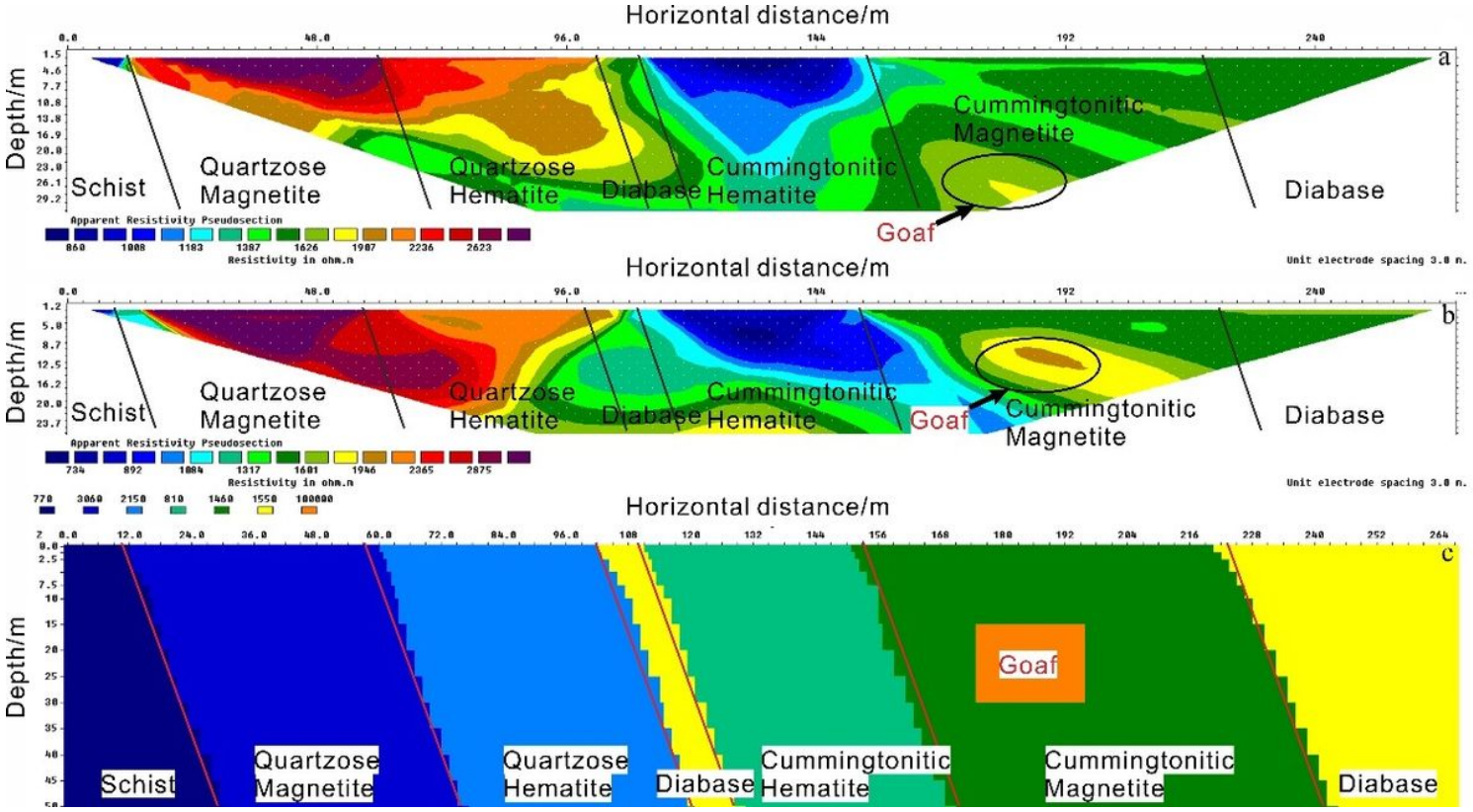

Figure 5

Survey model with caves in cummingtonitic magnetite.

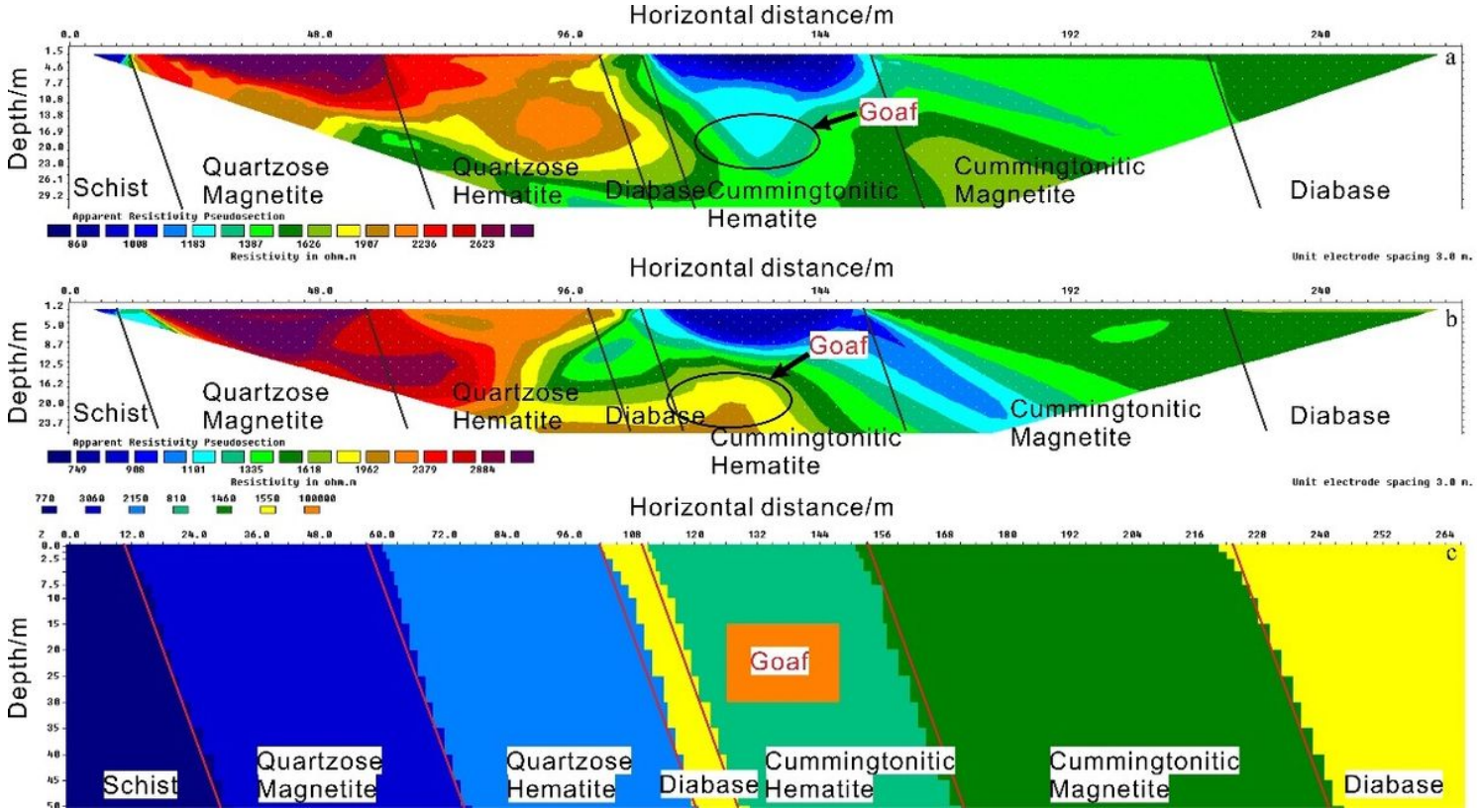

Figure 6

Survey model with caves in cummingtonitic hematite.

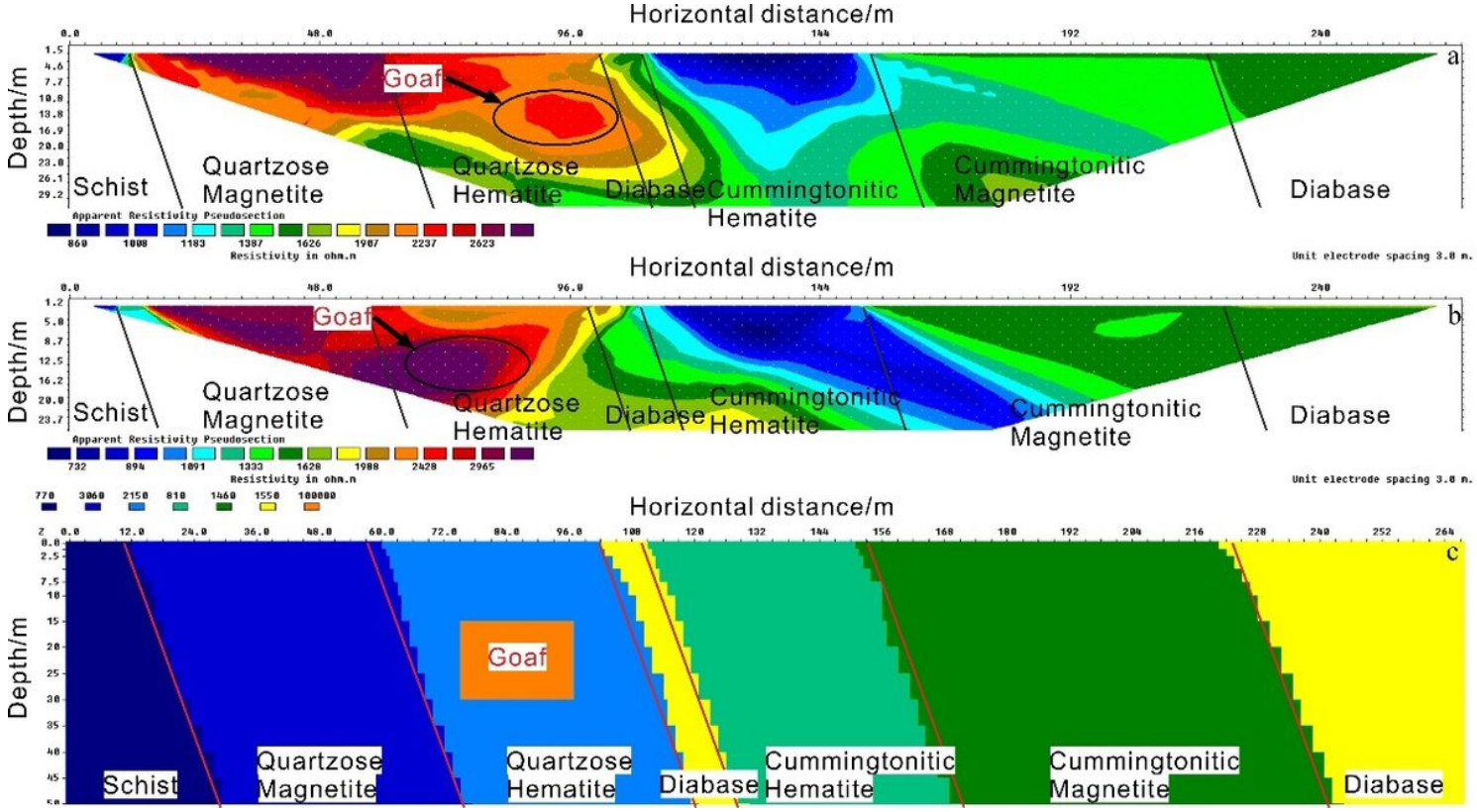

Figure 7

Survey model with caves in quartzose hematite.

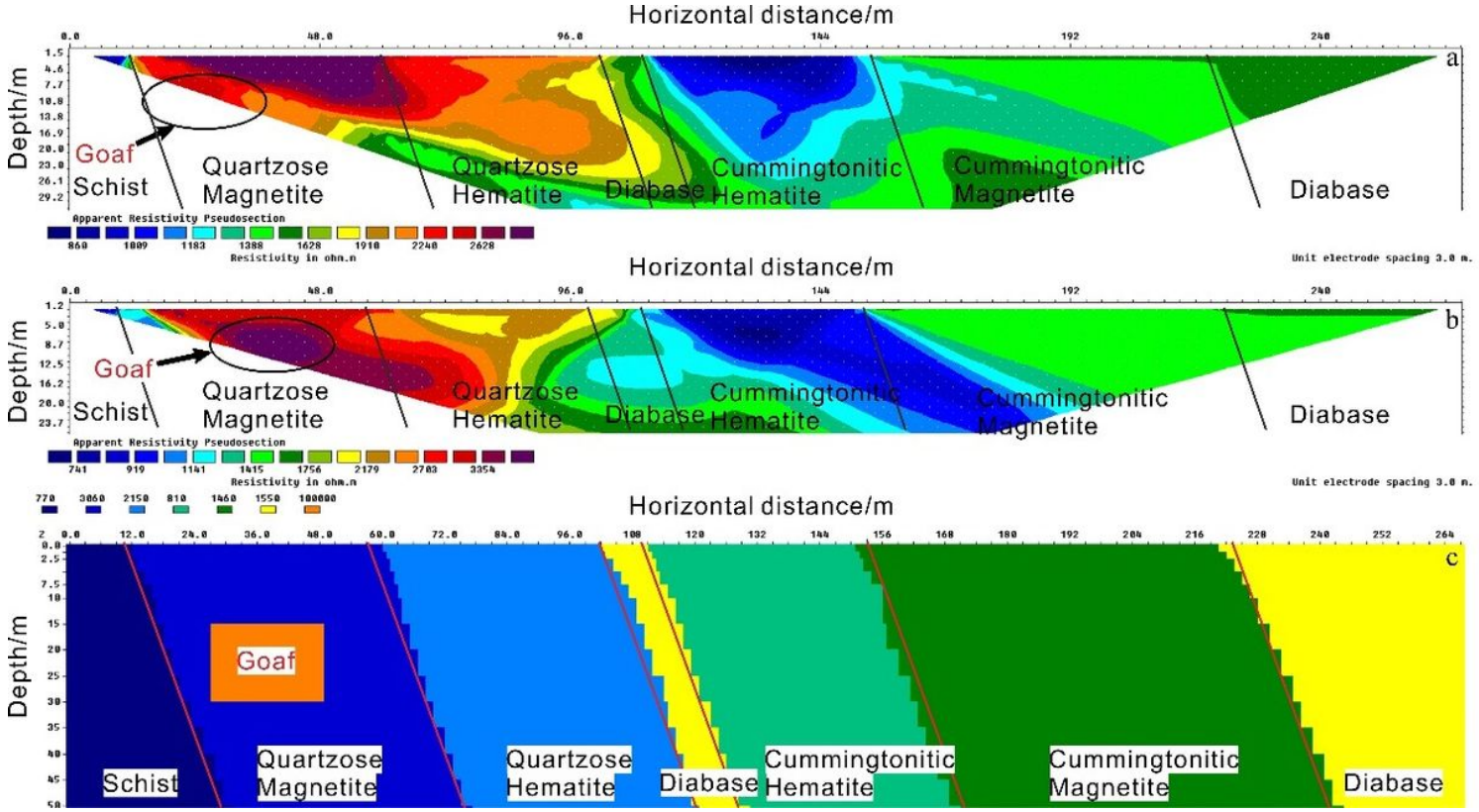

Figure 8

Survey model with caves in quartzose magnetite.

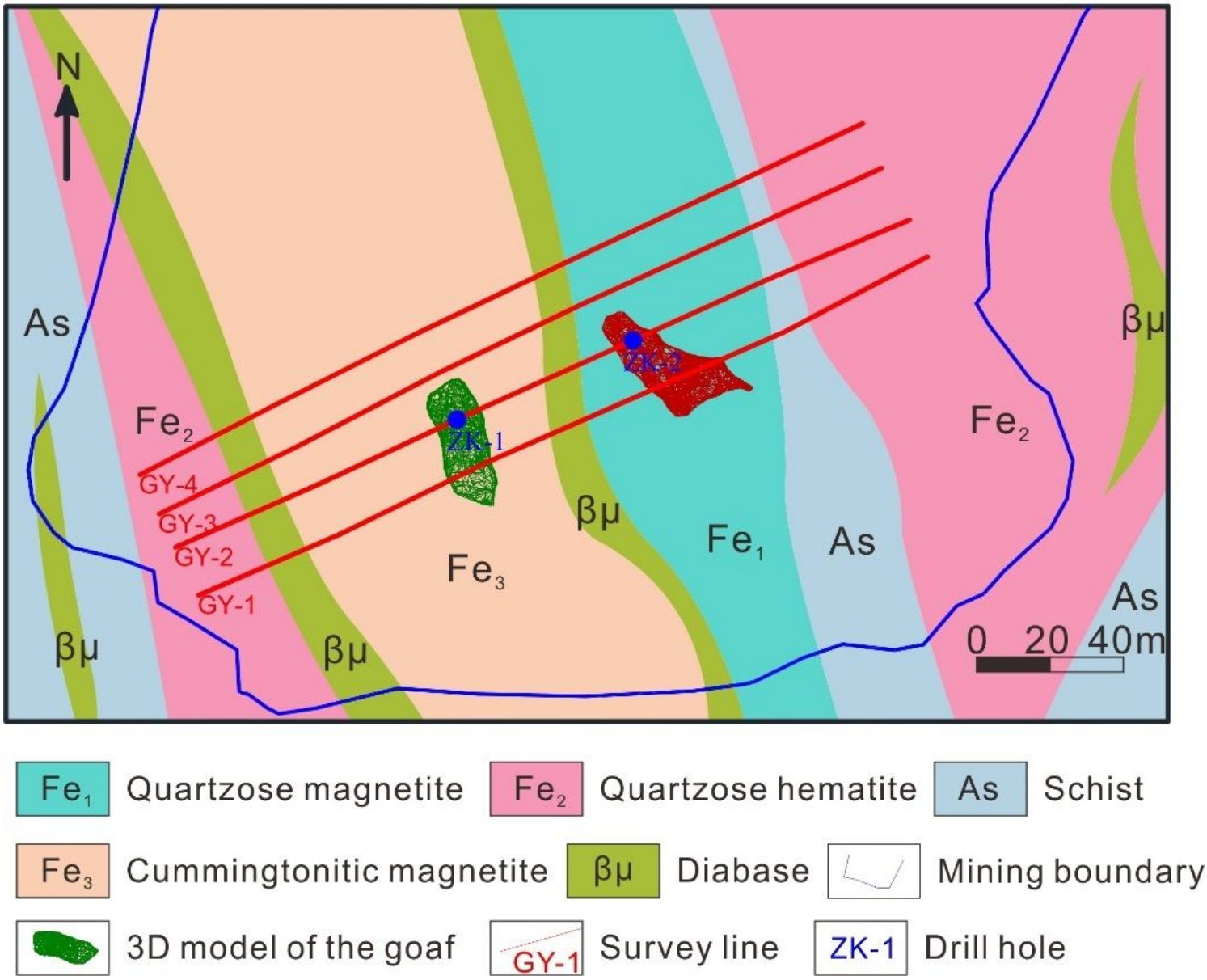

Figure 9

Survey line layout of the high-density resistivity method.

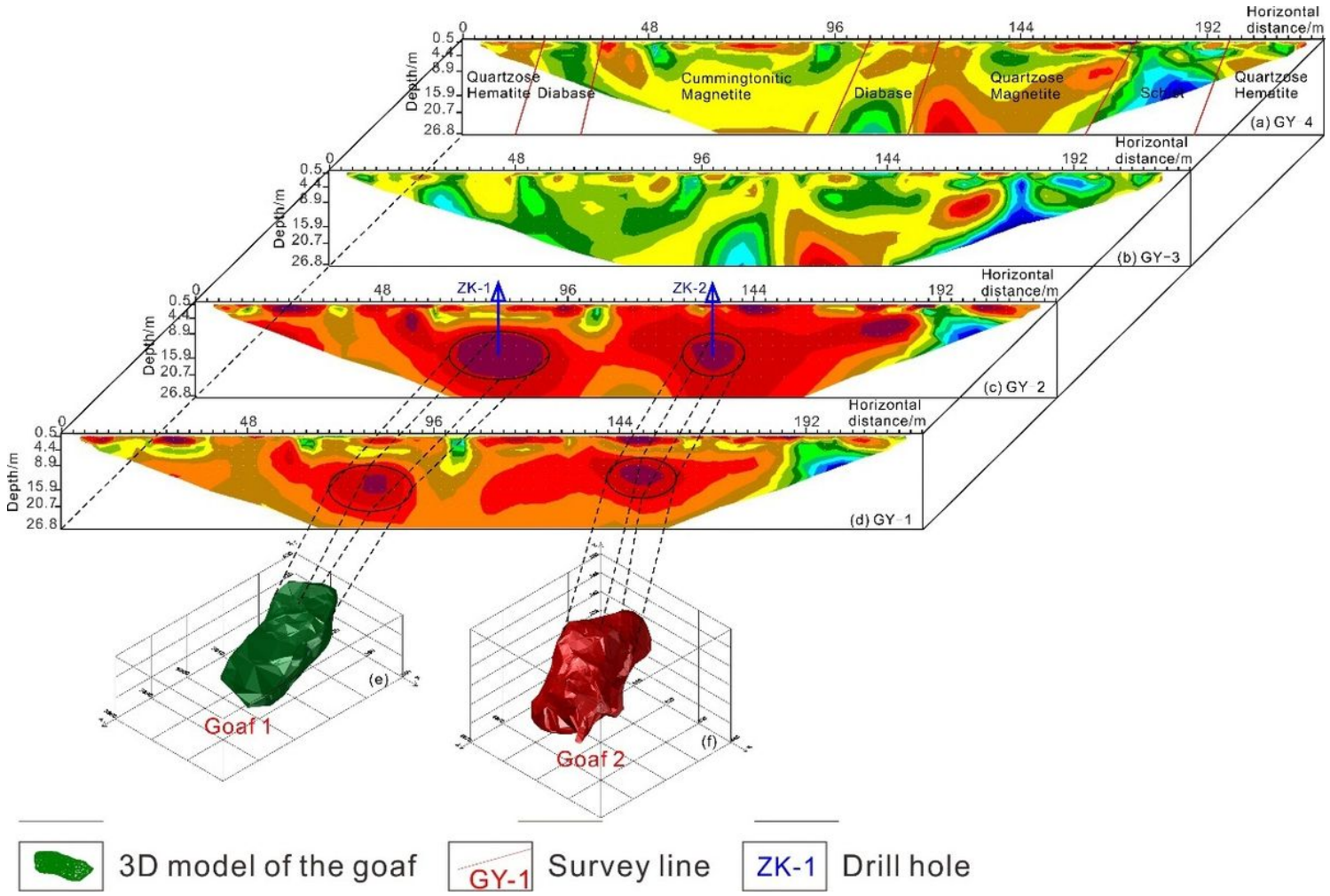

Figure 10

Resistivity inversion section of each survey line.